

# Can DFT Accurately Predict Spin Densities? Analysis of Discrepancies in Iron Nitrosyl Complexes

Katharina Boguslawski,<sup>†</sup> Christoph R. Jacob,<sup>\*,‡</sup> and Markus Reiher<sup>\*,†</sup>

<sup>†</sup>ETH Zurich, Laboratorium für Physikalische Chemie, Wolfgang-Pauli-Strasse 10, 8093 Zurich, Switzerland

<sup>‡</sup>Karlsruhe Institute of Technology (KIT), Center for Functional Nanostructures, Wolfgang-Gaede-Strasse 1a, 76131 Karlsruhe, Germany

 Supporting Information

**ABSTRACT:** Iron nitrosyl complexes are a particularly challenging case for density functional theory. In particular, for the low-spin state, different exchange–correlation functionals yield very different spin densities [Conradie, J.; Ghosh, A. *J. Phys. Chem. B* **2007**, *111*, 12621–12624]. Here, we investigate the origin of these differences in detail by analyzing the Kohn–Sham molecular orbitals. Furthermore, to decide which exchange–correlation functionals yield the most accurate spin densities, we make comparisons to CASSCF calculations. To ensure that the spin densities are converged with respect to the size of the active space, this comparison is performed for  $[\text{Fe}(\text{NO})]^{2+}$  as a model system. We find that none of the investigated exchange–correlation functionals are able to reproduce the CASSCF spin densities accurately.

## 1. INTRODUCTION

Transition metal complexes are central to metal-mediated catalysis and bioinorganic chemistry.<sup>1,2</sup> For a detailed understanding of their function as catalytically active centers and of catalytic mechanisms, theoretical analysis has become indispensable.<sup>3–12</sup> However, to reliably accomplish such an analysis remains a challenge for theoretical chemistry.<sup>13</sup>

In quantum chemical studies of transition metal complexes, usually density functional theory (DFT) is employed. But, especially, the treatment of open-shell systems remains a challenge to DFT.<sup>13,14</sup> In particular, results regarding the relative energetic ordering of closely lying states of different spin multiplicities are difficult to obtain with sufficient accuracy.<sup>13,15–26</sup> The performance of different approximate exchange–correlation functionals was intensely discussed in the literature.<sup>25–34</sup> Recently, Conradie and Ghosh have identified a particularly difficult case. They studied the spin-state energetics for the spin-crossover complex  $\text{Fe}(\text{salen})(\text{NO})$  as well as the  $\text{Fe}(\text{porphyrin})(\text{NO})$  complex.<sup>31</sup> These compounds feature a noninnocent nitric oxide ligand, and the resulting nitrosyl complexes exhibit a complicated electronic structure.<sup>30–32</sup> In addition to the inconclusive prediction of the correct ground state, notable differences in the spin density distributions were found with different exchange–correlation functionals. A detailed analysis of the sources of these differences, however, was not undertaken. Here, we pursue closing this gap by analyzing their origin. Moreover, we expand the DFT studies of Conradie and Ghosh by considering the BP86, TPSS, TPSSh, and M06-L exchange–correlation functionals as well.

According to the Hohenberg–Kohn theorem,<sup>35</sup> only the total electron density is required to predict the electronic energy as well as all other molecular observables. In principle, the spin density is not needed. However, for open-shell molecules, one usually introduces the spin density as an additional variable,

resulting in a spin-DFT formalism,<sup>36</sup> first proposed by von Barth and Hedin.<sup>37</sup> This allows one to construct better approximations for the exchange–correlation energy functional, since the additional information on the spin density is available and can be exploited. Within such a spin-DFT formalism, the exact spin-dependent exchange–correlation functional will (in addition to the exact electron density) also yield the exact spin density (see, e.g., ref 38), provided an unrestricted Kohn–Sham formalism is used.<sup>39</sup> Therefore, the spin density is one of the fundamental quantities in spin-DFT, and it is crucial to know which of the approximate exchange–correlation functionals yield accurate spin densities. Moreover, since electron paramagnetic resonance (EPR) parameters are explicitly dependent on the spin density,<sup>40</sup> reliable spin density distributions are an essential ingredient for an accurate calculation of EPR properties, which represents a difficult task for theoretical chemistry.<sup>41–45</sup>

With approximate exchange–correlation functionals, open-shell molecules in low-spin states are often treated in a broken-symmetry DFT formalism. In this case, the calculations do not yield the correct spin density. Instead, it has been argued that the Kohn–Sham reference system should represent the on-top pair density.<sup>46</sup> However, if properties depending on the spin-density such as EPR parameters are required, a broken-symmetry formalism is not useful. Therefore, we prefer the point of view that the need for a broken-symmetry treatment is an avoidable consequence of the insufficiencies of the currently available approximate exchange–correlation functionals and that instead one should aim at improved functionals that reproduce the exact spin-density.

To decide which exchange–correlation functional yields reliable spin densities, accurate benchmark calculations of the

Received: November 1, 2010

Published: August 15, 2011

spin density distribution are necessary. This requires multi-reference methods such as the multiconfigurational complete-active-space self-consistent-field (CASSCF) approach. The unfavorable scaling in computing time with the size of the active orbital space, however, disfavors the description of large molecular systems, and hence, such correlation methods are not frequently used in theoretical investigations of transition metal complexes (for counterexamples, see refs 32, 47, 48). Detailed CASSCF studies of the salen- as well as of different porphyrin-containing iron nitrosyl complexes were recently performed by Pierloot et al.<sup>32,49</sup> These studies provided important insight into the electronic structure of these compounds and the energetics of the different spin states. Furthermore, the problem of the inconclusive picture provided by DFT calculations for the spin densities was also addressed. A comparison of Mulliken spin populations and of spin density isosurface plots indicated that the nonhybrid functionals yield the most accurate spin densities.

However, a more detailed comparison of the DFT and the CASSCF calculations was not performed. Furthermore, the large size of the molecules under study restricts the dimension of the active space, and it is therefore not clear whether the spin densities are converged with respect to the size of the active space.

To circumvent these restrictions, one needs a small model system for which similar differences in the spin density distributions are found in DFT calculations, but where, due to the small size of this model system, one is still able to ascertain how the choice of the active space affects the resulting spin density distributions. Such an analysis of the spin density could then validate the corresponding CASSCF reference spin densities. Furthermore, a more detailed examination of the spin density distributions by considering the DFT–CASSCF spin density differences could be used as a representative benchmark of the approximate exchange–correlation functionals.

This work is organized as follows. In section 2, the computational details are presented. A detailed discussion of DFT spin densities of iron nitrosyl complexes is given in section 3. Then, section 4 introduces  $[\text{Fe}(\text{NO})]^{2+}$  as a small model system and validates the quality of CASSCF reference spin densities as a benchmark for the DFT results. Finally, a summary and concluding remarks are given in section 5.

## 2. COMPUTATIONAL METHODOLOGY

All unrestricted Kohn–Sham DFT calculations were performed with the quantum chemical program package ADF.<sup>50</sup> Eight popular exchange–correlation functionals were employed, from the widely used B3LYP hybrid exchange–correlation functional with 20% exact exchange<sup>51</sup> and TPSSh<sup>52</sup> with 10% Hartree–Fock exchange to five pure exchange–correlation functionals: OLYP,<sup>53</sup> OPBE,<sup>54,55</sup> BP86,<sup>56,57</sup> BLYP,<sup>56,58</sup> TPSS,<sup>59</sup> and M06-L.<sup>60</sup> For the molecular structures of  $\text{Fe}(\text{salen})(\text{NO})$  (in its two different conformations) and  $\text{Fe}(\text{porphyrin})(\text{NO})$ , the optimized coordinates calculated by Conradie and Ghosh were taken.<sup>31</sup> For direct comparison, all DFT spin density profiles were obtained from single point calculations at these optimized structures. Since Slater-type orbitals give consistent and rapidly converging results for spin state splittings,<sup>61</sup> we applied a triple- $\zeta$  plus polarization Slater-type orbital basis set (TZP). The SCF algorithm was considered converged if the largest element of the commutator of the Fock matrix and the density matrix represented in the basis functions was lower than  $10^{-6}$  Hartree. The

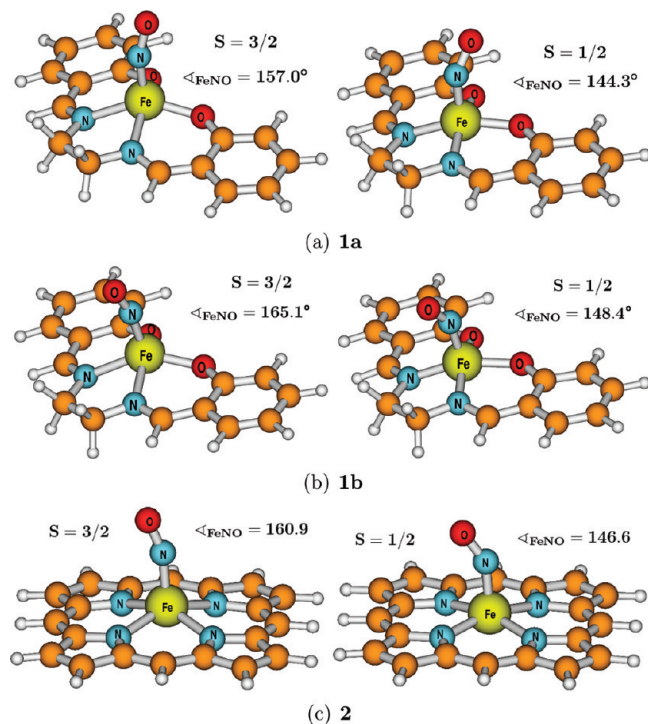


**Figure 1.** Structures of the iron nitrosyl complexes investigated in this work. (a) Conformation a of  $\text{Fe}(\text{salen})(\text{NO})$ . (b) Conformation b of  $\text{Fe}(\text{salen})(\text{NO})$ . (c)  $\text{Fe}(\text{porphyrin})(\text{NO})$ . All structures are taken from ref 31.

spin density distributions were visualized using the ADF–GUI ADFVIEW program.<sup>62</sup>

All CASSCF calculations were performed with the program package Molpro<sup>63</sup> using Dunning's cc-pVTZ basis set for all atoms.<sup>64,65</sup> As an initial guess, an unrestricted Hartree–Fock calculation was performed. The natural orbitals from this unrestricted Hartree–Fock calculation are then used as starting orbitals for the CASSCF procedure. As convergence criteria, an orbital gradient threshold of  $10^{-2}$  atomic units was chosen, and the threshold for the change in total energy was set to  $10^{-6}$  Hartree in all calculations. As an optimization method, the method developed by Werner, Meyer, and Knowles<sup>66–68</sup> was used in all calculations. The CASSCF spin densities were visualized using the program MOLEKEL.<sup>69</sup>

## 3. SPIN DENSITIES OF IRON NITROSYL COMPLEXES

Following the work of Ghosh and Conradie,<sup>31</sup> we investigate two iron nitrosyl complexes, denoted as  $\{\text{FeNO}\}^7$  after Enemark and Feltham<sup>70</sup> (this notation indicates that seven electrons are distributed among the combinations of the NO  $\pi^*$  and the Fe 3d orbitals):  $\text{Fe}(\text{salen})(\text{NO})$  (**1**) and  $\text{Fe}(\text{porphyrin})(\text{NO})$  (**2**), whereby the former occurs in two different conformations named **1a** and **1b** (see Figure 1). The unpaired electron from the neutral NO species and the six d electrons of Fe(II) can be distributed over the combinations of the Fe 3d and NO  $\pi^*$  orbitals. The most favorable spin states resulting from this electronic structure are a doublet (one unpaired electron) and a quartet (three unpaired electrons) state. Experimentally, **2** is known to possess a doublet ( $S = 1/2$ ) ground state,<sup>71,72</sup> while **1** exhibits a thermal spin-crossover from the doublet ( $S = 1/2$ ) to the quartet state ( $S = 3/2$ ) near 175 K.<sup>73</sup> Therefore, we

considered only the doublet and quartet spin states for all iron nitrosyl complexes in our theoretical study.

**3.1. Energetics.** We first analyze the relative spin-state energies of the iron nitrosyl complexes. These are listed, for the exchange–correlation functionals considered, in Table 1. For **1** (in both conformations), we found adiabatic energy splittings between the quartet and doublet state in the range of +12 and −10 kcal/mol. It is obvious that the energy splitting is largely dependent on the amount of exact exchange encoded in the exchange–correlation functional.<sup>26</sup> B3LYP (with 20% exact exchange) yields a quartet ground state favored by about 9 kcal/mol, while for TPSSh (with only 10% exact exchange), doublet and quartet spin states of almost the same energy are obtained. OLYP and OPBE behave similar to TPSSh and yield  $S = 1/2$  and  $S = 3/2$  spin states that are similar in energy. This is in agreement with the experimentally observed spin-crossover behavior. In contrast to the hybrid functionals, TPSS, BP86, and BLYP (all pure functionals without exact exchange) favor the doublet over the quartet state by approximately 10 kcal/mol. An exception is the meta-GGA functional M06-L (also a pure functional without exact exchange), which behaves similarly to B3LYP and favors the quartet state by about 9 kcal/mol. We note that the relative energies for OLYP, OPBE, and BLYP are consistent with the previous work presented by Conradie and Ghosh.<sup>31</sup> In general, only small deviations (<0.2 kcal/mol) can be observed. However, larger differences from the results of

Conradie and Ghosh are found for **1b** for OPBE and B3LYP (2.1 and −11.1 kcal/mol, respectively). The reason for these differences can be revealed by inspecting the Mulliken spin populations and charges in our calculations (see Table 1 in the Supporting Information) and in ref 31. Note that since we use the same basis sets as in ref 31, these can be compared directly. The comparison indicates that Conradie and Ghosh have found a different state for  $S = 3/2$  (OPBE) and  $S = 1/2$  (B3LYP). Further, comparing the energies of these different states shows that those found in this work are lower in energy, and the corresponding Mulliken charges are physically more reasonable with no negative charges on the iron atom. For **1a**, larger differences can be observed for B3LYP. However, the Mulliken spin populations and charges in our calculations are similar to those in ref 31, and the origin of these differences remains unclear.

For **2**, similar observations can be made. The adiabatic energy splittings follow the same trend as observed for **1**, except that the corresponding energy splittings are 6 kcal/mol higher in energy and, thus, found between −3 and +18 kcal/mol. B3LYP and M06-L predict a quartet ground state by about 3 kcal/mol. All other exchange–correlation functionals studied yield a doublet ground state, but with different relative energies. OLYP and OPBE as well as TPSSh favor the doublet state by 6 kcal/mol, while TPSS, BP86, and BLYP yield an energy gap of approximately 17 kcal/mol. As for **1**, our results for OLYP and OPBE are consistent with the previous work of Conradie and Ghosh,<sup>31</sup> and in general, only small deviations can be observed. Larger differences are only found for B3LYP. Again, inspection of the Mulliken spin populations (given in Table 2 of the Supporting Information) and charges indicates that a different state was converged for  $S = 1/2$ , and in comparison to ref 31, the one found by us is lower in energy.

**3.2. Spin Density Distributions.** It was already pointed out by Ghosh and Conradie<sup>30,31</sup> that the spin density distributions for the iron nitrosyl complexes are strongly dependent on the choice of the exchange–correlation functional. Let us first have a closer look at the spin density profiles before we continue to elaborate on the sources of these differences in detail.

The spin density distributions for **1b** are displayed in Figure 2. The spin densities for the quartet state do not depend on the exchange–correlation functional, where the iron atom carries an excess of  $\alpha$ -electron density and the nitrosyl ligand an excess of

**Table 1. Energy Differences ( $E^{S=(3/2)} - E^{S=(1/2)}$ ) between Quartet and Doublet State (kcal/mol) in a TZP Basis Set for Selected Exchange–Correlation Functionals<sup>a</sup>**

	OLYP	OPBE	BP86	BLYP	TPSS	TPSSh	B3LYP	M06-L
<b>1a</b>	−1.0	0.6	10.5	8.8	11.2	1.3	−9.0	−9.6
<b>1a</b> <sup>31</sup>	−1.2	0.5		8.8			−9.5	
<b>1b</b>	0.3	1.6	11.7	9.8	12.2	1.2	−9.7	−8.9
<b>1b</b> <sup>31</sup>	0.4	2.1		9.7			−11.1	
<b>2</b>	5.7	6.2	17.0	16.2	17.6	6.6	−3.1	−2.5
<b>2</b> <sup>31</sup>	5.9	6.5		16.6 <sup>b</sup>			−4.6	

<sup>a</sup> A negative energy difference indicates that the quartet state ( $S = 3/2$ ) is more stable, while for a positive value the doublet state ( $S = 1/2$ ) is preferred. For comparison, the values reported by Conradie and Ghosh in ref 31 are also included. <sup>b</sup> Structure optimization.

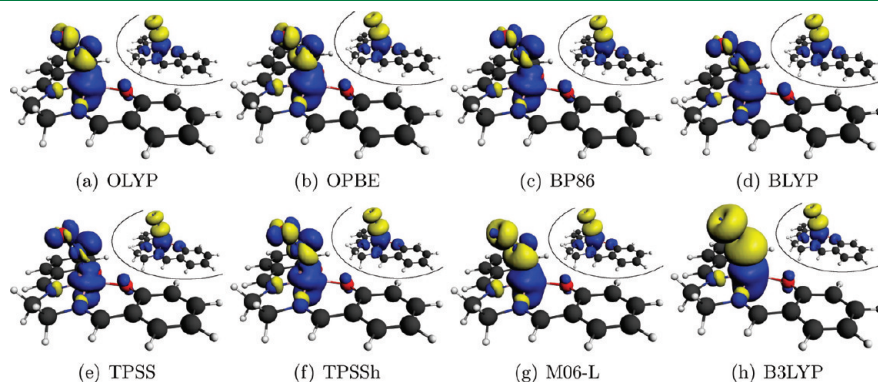


**Figure 2.** Spin density profiles for **1b** in a TZP basis set for selected density functionals. An isosurface value of 0.003 is chosen. The small picture in the upper right corner shows the quartet spin density for each exchange–correlation functional, while the large picture displays the sensitive doublet spin density. The blue surface (positive spin density) corresponds to an excess of  $\alpha$ -electron density, while the yellow surface (negative spin density) corresponds to an excess of  $\beta$ -electron density.

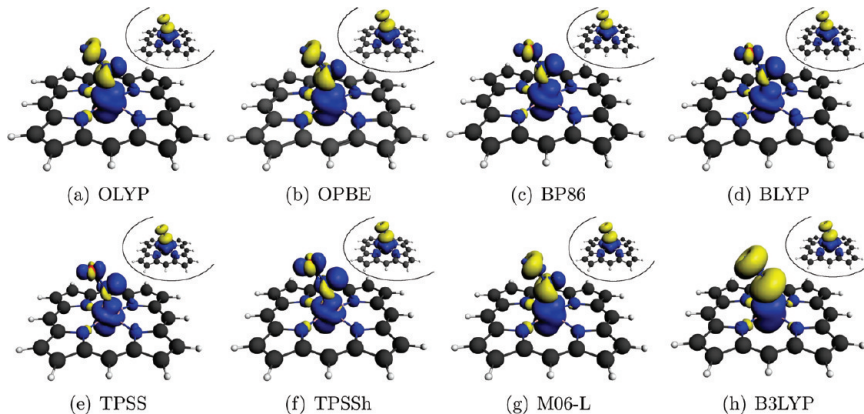


**Figure 3.** Spin density profiles for **2** in a TZP basis set for selected density functionals. An isosurface value of 0.003 is chosen. The small picture in the upper right corner shows the quartet spin density for each exchange–correlation functional, while the large picture displays the sensitive doublet spin density. The blue surface (positive spin density) corresponds to an excess of  $\alpha$ -electron density, while the yellow surface (negative spin density) corresponds to an excess of  $\beta$ -electron density.

$\beta$ -electron density. For the doublet state, however, notable differences in the spin density distributions can be observed. The spin densities can be ordered according to their associated energy splittings obtained for different exchange–correlation functionals. For BP86, BLYP, and TPSS, the spin densities are similar. OLYP, OPBE, and TPSSh yield different distributions around the nitrosyl ligand atoms with a larger amount of  $\beta$ -electron density. This excess of  $\beta$ -electron density further increases for M06-L. A completely different picture is obtained for B3LYP. While for all other functionals there is both  $\alpha$ - and  $\beta$ -electron density on the nitrosyl ligand, with B3LYP, the ligand carries only  $\beta$ -electron density. In addition, the amount of  $\beta$ -electron density on the nitrosyl ligand is much larger with B3LYP than for all the other functionals, as is also obvious from the Mulliken spin populations (see Table 1 in the Supporting Information). For **1a**, similar spin density distributions are obtained, which are shown in Figure 1 in the Supporting Information.

Figure 3 shows the calculated spin densities for **2** as obtained with different exchange–correlation functionals. As already observed for **1**, BP86, BLYP, and TPSS yield similar results. One can recognize an increase in the  $\alpha$ -electron density at the ligand atoms for TPSSh, and its decrease around the iron center. OLYP, OPBE, and M06-L yield a large amount of  $\beta$ -electron density located around the nitrosyl ligand atoms, which is missing for BP86, BLYP, TPSS, and TPSSh. As for **1**, an excess of  $\beta$ -electron density only on the nitrosyl ligand is found for B3LYP. But in contrast to **1**, we observe that calculations with different exchange–correlation functionals which yield similar energy splittings result in different spin density distributions (e.g., TPSSh which is comparable in relative energy, but not in spin density to OLYP/OPBE). M06-L, on the other hand, delivers a spin density similar to OLYP and OPBE but yields a very different energy gap ( $-2.5$  kcal/mol with M06-L vs  $6$  kcal/mol with OLYP/OPBE).

**3.3. Origin of Deviations in the Spin Density.** To understand the origin of the differences in the spin densities of the doublet state, we investigate the Kohn–Sham molecular orbitals. For this, we choose **1b** and the three exchange–correlation functionals, BP86, OLYP, and B3LYP. To elucidate the subsequent analysis of the DFT orbitals, it is instructive to consider the qualitative molecular orbital diagram introduced by Hoffmann

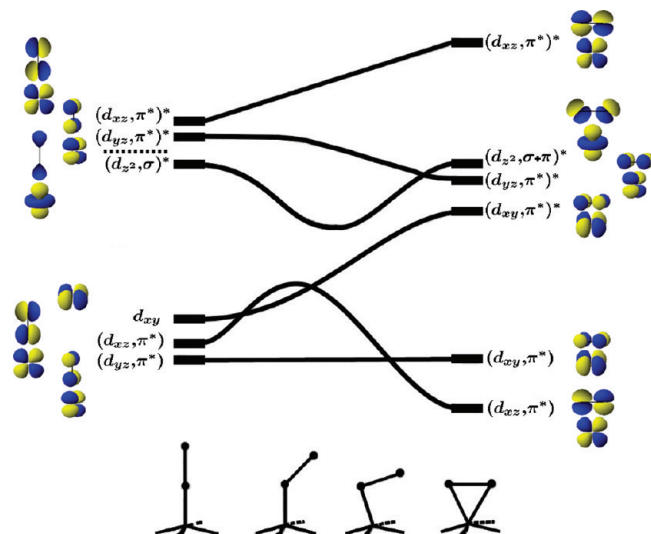


**Figure 4.** Hoffmann's correlation diagram for pentacoordinate metal complexes as presented in ref 74.

et al. for pentacoordinate metal complexes,<sup>74,75</sup> which we depict in Figure 4.

In their qualitative approach, they considered the iron  $d_{xy}$ ,  $d_{z^2}$ ,  $d_{xz}$ , and  $d_{yz}$  orbitals (the  $d_{x^2-y^2}$ -orbital is excluded because it is significantly higher in energy) as well as the NO  $\sigma$  and the two NO  $\pi^*$  orbitals. Four ligands (in our case, the nitrogen and oxygen donor atoms of the salen ligand and the nitrogen donor atoms of the porphyrin ligand) are arranged in the  $xy$  plane along the coordinate axes. Above this  $xy$  plane, the NO ligand is located between the  $xz$  and  $yz$  planes. For the bent structure present in **1** and **2**, these form (due to symmetry considerations) the molecular orbitals  $(d_{yz}, \pi^*)$ ,  $(d_{xz}, \pi^*)$ ,  $d_{xy}$ ,  $(d_{z^2}, \sigma)^*$ ,  $(d_{yz}, \pi^*)$ , and  $(d_{xz}, \pi^*)$ , which are occupied by seven electrons for the  $\{\text{FeNO}\}^7$  complexes. For the doublet state, the  $(d_{yz}, \pi^*)$ ,  $(d_{xz}, \pi^*)$ , and  $d_{xy}$  orbitals are doubly occupied, and the  $(d_{z^2}, \sigma)^*$  orbital is singly occupied. These orbitals, in particular the singly occupied  $(d_{z^2}, \sigma)^*$  orbital, determine the spin density distributions, and the corresponding differences in spin densities can be traced back to differing orbital patterns.

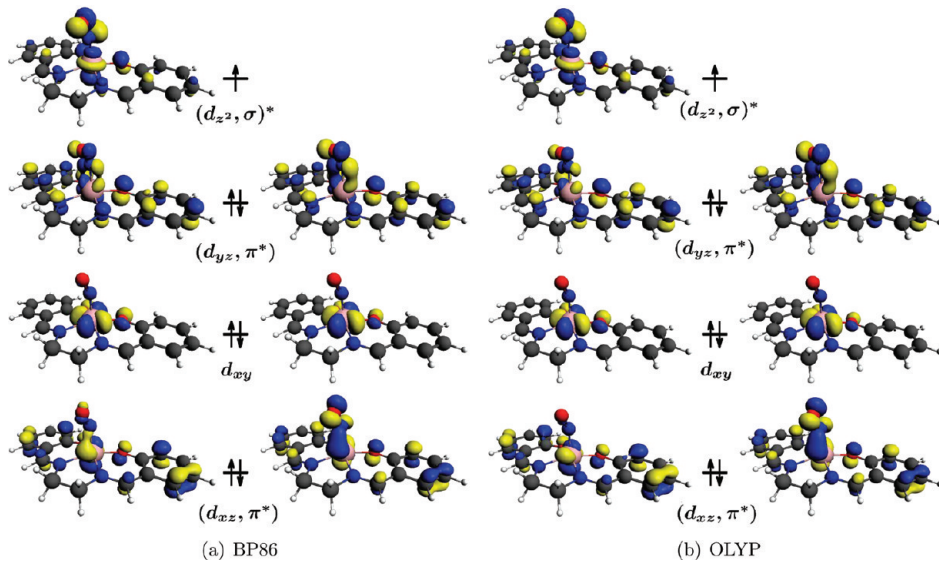


**Figure 5.** Valence orbitals for the doublet state of **1b** in a TZP basis set for selected exchange–correlation functionals. Those  $\alpha$  and  $\beta$  orbitals which correspond to the same orbital combination are grouped together and ordered qualitatively according to the energy of the corresponding  $\alpha$  orbital. An isosurface value of 0.05 is chosen. Only the orbitals which determine the spin density distribution are shown. Orbitals for  $\alpha$  electrons are displayed on the left-hand side and orbitals for  $\beta$  electrons on the right-hand side.

For the quartet state, the  $(d_{yz}, \pi^*)$  and  $(d_{xz}, \pi^*)$  orbitals are doubly occupied. The remaining three electrons are then distributed over the singly occupied  $d_{xy}$ ,  $(d_{z^2}, \sigma)^*$ , and  $d_{x^2-y^2}$  orbitals. Note that, in this case, the order of the molecular orbitals changes, and  $d_{x^2-y^2}$ , which is not shown in Figure 4, has to be included. The orbitals obtained in the DFT calculations for the quartet state are similar for all exchange–correlation functionals and qualitatively agree with Hoffmann’s simplified picture. As a representative example, the relevant orbitals from the BP86 calculation are shown in Figure 2a in the Supporting Information.

Figure 5 shows the highest occupied molecular orbitals obtained for the doublet state with OLYP and BP86. All orbitals are described by Hoffmann’s qualitative molecular orbital picture. However, in the unrestricted Kohn–Sham DFT calculations,  $\alpha$  and  $\beta$  orbitals are different. In particular, the  $(d_{xz}, \pi^*)$  orbital contains no significant contribution from the NO  $\pi^*$  orbital to the corresponding  $\alpha$  orbital. This induces an excess of  $\beta$ -electron density around the NO fragment. The same can be observed for the  $(d_{yz}, \pi^*)$  orbital, where the contribution of the NO  $\pi^*$  orbital to the  $\alpha$  orbitals is reduced. The excess of  $\alpha$ -electron density around the iron atom and nitrosyl fragment can be attributed to the singly occupied  $(d_{z^2}, \sigma)^*$  orbital. Furthermore, there are also orbital contributions from the salen (and porphyrin) ligands, which, however, do not contribute to the spin density. In the case of OLYP, the  $\alpha$ -spin  $(d_{yz}, \pi^*)$  orbital contains less contribution from the NO  $\pi^*$  orbital as compared to BP86, which increases the  $\beta$ -electron density around the nitrosyl fragment (see also Figure 2) and induces the divergent spin density distributions.

For B3LYP, we observe different orbital shapes for  $\alpha$  and  $\beta$  electrons as compared to the former exchange–correlation functionals (see Figure 6). The  $\alpha_1$  and  $\alpha_2$  and the  $\beta_1$  and  $\beta_2$  orbitals result in very different orbital combinations, while the  $\alpha_3$  and  $\alpha_4$  and the  $\beta_3$  orbitals can be related to Hoffmann’s orbital diagram of Figure 4. The nonbonding  $d_{xy}$  orbital ( $\alpha_2$  and  $\beta_2$ ) is replaced by different combinations of Fe d and NO  $\pi^*$  orbitals, which results in a stronger distribution of  $\beta$ -electron density into

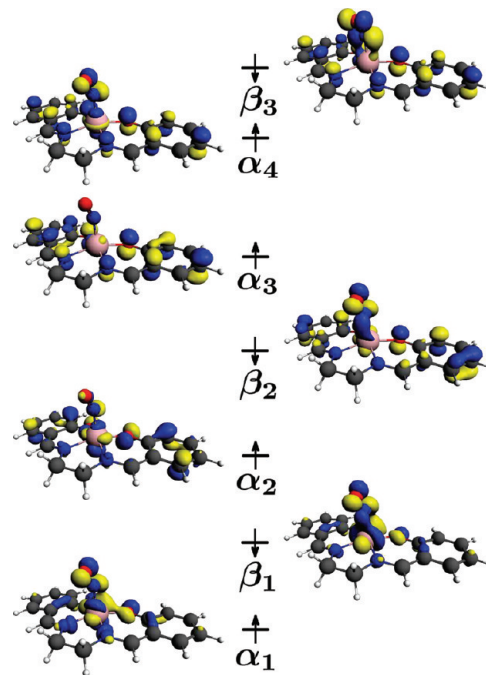


**Figure 6.** Valence orbitals for **1b** in a TZP basis set for B3LYP ordered qualitatively according to their energy. An isosurface value of 0.05 is chosen. Only the orbitals which determine the spin density distribution are shown. Orbitals for  $\alpha$  electrons are displayed on the left-hand side and orbitals for  $\beta$  electrons on the right-hand side.

the NO  $\pi^*$  orbitals. While  $\alpha$  electrons are preferentially distributed over the iron center and the salen fragment ( $\alpha_2$  and  $\alpha_3$ ),  $\beta$  electrons occupy the NO  $\pi^*$  orbitals ( $\beta_2$  and  $\beta_3$ ). This generates the characteristic cylindrical shape of the  $\beta$  electron density for B3LYP. Moreover, two singly occupied  $\alpha$  orbitals and two different singly occupied  $\beta$  orbitals are obtained (compare  $\alpha_1/\alpha_2$  and  $\beta_1/\beta_2$ , respectively).

**Table 2.**  $\langle \hat{S}^2 \rangle$  Expectation Values in a TZP Basis Set for a Given Exchange–Correlation Functional

	OLYP	OPBE	BP86	BLYP	TPSS	TPSSh	B3LYP	M06-L	ideal
<b>1a</b> $\langle \hat{S}_{\text{hs}}^2 \rangle$	4.40	4.42	4.21	4.18	4.27	4.57	4.75	4.62	3.75
$\langle \hat{S}_{\text{ls}}^2 \rangle$	0.83	0.83	0.78	0.77	0.78	0.92	1.29	0.91	0.75
<b>1b</b> $\langle \hat{S}_{\text{hs}}^2 \rangle$	4.40	4.42	4.21	4.19	4.27	4.58	4.75	4.63	3.75
$\langle \hat{S}_{\text{ls}}^2 \rangle$	0.80	0.81	0.77	0.77	0.77	0.82	1.26	0.87	0.75
<b>2</b> $\langle \hat{S}_{\text{hs}}^2 \rangle$	4.35	4.37	4.18	4.16	4.23	4.50	4.67	4.56	3.75
$\langle \hat{S}_{\text{ls}}^2 \rangle$	0.81	0.82	0.77	0.77	0.77	0.80	1.20	0.86	0.75
<b>3</b> $\langle \hat{S}_{\text{hs}}^2 \rangle$	4.49	4.53	4.35	4.30	4.41	4.68	4.82	4.68	3.75
$\langle \hat{S}_{\text{ls}}^2 \rangle$	0.95	0.97	0.83	0.82	0.82	1.24	1.48	1.01	0.75

These different occupational patterns and orbital shapes result in a “broken-symmetry-like” solution for B3LYP, which can also be seen in the significantly larger  $\langle \hat{S}^2 \rangle$  expectation value of 1.2 as compared to an ideal value of 0.75 in Hartree atomic units (see also Table 2; the same holds for 2). However, even though broken-symmetry solutions often yield accurate energetics, they result in incorrect spin density distributions. While this is obvious when broken-symmetry solutions are employed for singlet states (where the correct spin density vanishes<sup>14</sup>), for the doublet state considered here, it is less clear whether the spin density obtained from a particular solution is physically meaningful or not. Obviously, this is a serious problem if one is interested in the calculation of EPR properties. Note again that with the exact spin-dependent exchange–correlation functional, a broken-symmetry treatment should not be required, and unrestricted Kohn–Sham DFT would always yield the exact spin density.<sup>38,39</sup>

Finally, we note that the spin densities of 1 are comparable to those of 2 for a given exchange–correlation functional. Hence, similar spin densities are obtained for complexes with porphyrin or salen ligands. The iron nitrosyl moiety dominates the distribution of the  $\alpha$ - and  $\beta$ -electron density, and we will have a closer look at this fragment in section 4.

#### 4. DEFINING A SUITABLE MODEL FOR ACCURATE REFERENCE CALCULATIONS

Since the DFT spin densities are ambiguous, reference spin densities are required to decide which exchange–correlation functionals provide reliable spin densities. This task can be achieved by applying multireference *ab initio* methods. However, for the large salen and porphyrin complexes discussed above, such calculations are not feasible or require a restriction of the active space. Therefore, we construct a small model system for which CASSCF calculations are computationally feasible but which still shows similar differences in spin density distributions for the selected exchange–correlation functionals as the large iron nitrosyl complexes. As a model system, we choose  $[\text{FeNO}]^{2+}$  (3), since the FeNO moiety dominates the distribution of  $\alpha$  and  $\beta$  electrons in the full-fledged complexes. However, for the small  $[\text{FeNO}]^{2+}$  molecule, a structure optimization of the bent structure results in a linear orientation of the nitrosyl group, suggesting an Fe(I) center and a positively charged  $\text{NO}^+$  fragment. To ensure transferability, we need to enforce the occupation of the same orbitals as present in the large  $\{\text{FeNO}\}^7$  complexes. These problems can be solved by considering the fixed geometry of the bent iron nitrosyl fragment present in the larger  $\{\text{FeNO}\}^7$  complexes. Furthermore, we include four negative point charges of  $-0.5e$  each, which are located at a distance of

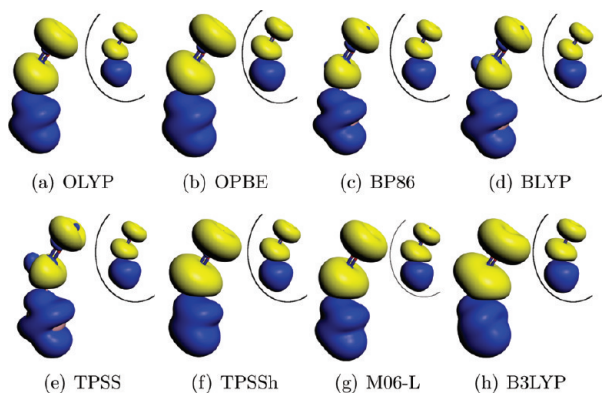


**Figure 7.** Spin density profiles for 3 in a TZP basis set for selected density functionals. An isosurface value of 0.003 is chosen. The small picture in the upper right corner shows the quartet spin density for each exchange–correlation functional, while the large picture displays the sensitive doublet spin density. The blue surface (positive spin density) corresponds to an excess of  $\alpha$ -electron density, while the yellow surface (negative spin density) corresponds to an excess of  $\beta$ -electron density.

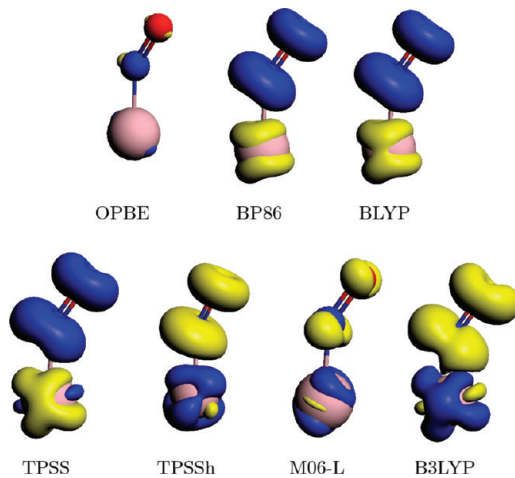


**Figure 8.** Spin density difference plots for 3 in a TZP basis set of the spin density profile for the corresponding exchange–correlation functional mentioned with respect to OLYP. An isosurface value of 0.003 is chosen. The blue surface corresponds to an excess of  $\alpha$ -electron density, while the yellow surface corresponds to an excess of  $\beta$ -electron density with respect to OLYP.

1.131 Å from the iron atom on the  $x$  and  $y$  axes, to model a square-planar ligand field and to obtain a similar electronic structure as present in the larger  $\{\text{FeNO}\}^7$  complexes. All following CASSCF calculations are performed in  $C_1$  symmetry and apply the OLYP optimized iron nitrosyl fragment of 1a.

**4.1. DFT Calculations.** First, we examine the influence of the exchange–correlation functional on the spin density distribution for the  $[\text{Fe}(\text{NO})]^{2+}$  model system. In Figure 7, the spin density profiles calculated for different exchange–correlation functionals are shown. As for the larger  $\{\text{FeNO}\}^7$  complexes, the spin densities for the quartet configuration (shown in the inset on the right for each functional) are similar. The spin densities of the doublet state are shown in Figure 7 on the left for each functional. Compared to those of 1 and 2, the differences between the different functionals appear smaller. However, there are considerable differences. To illustrate these more clearly, Figure 8

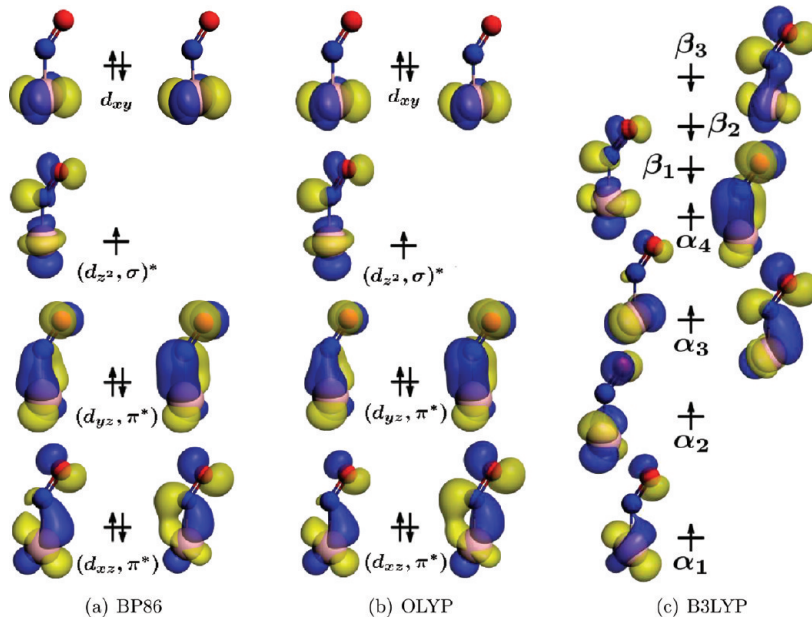


**Figure 9.** Valence orbitals of **3** in a TZP basis set for selected exchange–correlation functionals. An isosurface value of 0.05 is chosen. The orbitals are ordered qualitatively according to the energy of the corresponding  $\alpha$  orbital. Orbitals which correspond to the same orbital combination are grouped together. All other orbitals turned out to be similar in shape for all exchange–correlation functionals. Orbitals for  $\alpha$  electrons are displayed on the left-hand side and orbitals for  $\beta$  electrons on the right-hand side.

shows isosurface plots of the differences between the spin density obtained with OLYP and each of the other functionals. The isosurface value of 0.003 used in these plots of the spin density differences is the same as the one used for the spin densities themselves in Figure 7. Plots using larger isosurface values of 0.005 and 0.01 are shown in the Supporting Information (Figures 3 and 4) and are qualitatively similar to Figure 7.

The spin density difference plots reveal that for the  $[\text{Fe}(\text{NO})]^{2+}$  model system the spin densities can be arranged in two different groups, which are qualitatively similar to those found for **1** and **2**. For OLYP and OPBE, the spin density distributions are almost identical. The nonhybrid functionals BP86, BLYP, and TPSS lead to less  $\beta$ -electron density on the nitrosyl ligand compared to OLYP, i.e., a smaller overall spin polarization. For these functionals, one finds a region of  $\alpha$ -electron density near the nitrogen atom in Figure 7. As for **1** and **2**, M06-L and the hybrid functionals TPSSh and B3LYP yield a stronger spin polarization compared to OLYP, corresponding to more  $\alpha$ -electron density on the nitrosyl fragment in the difference plots of Figure 8. The magnitude of spin polarization, however, is dependent on the exchange–correlation functional and increases from M06-L to TPSSh and is largest for B3LYP.

In line with the spin density difference plot, the Mulliken spin populations given in Table 4 show the same increase in  $\beta$ -electron density on the nitrosyl ligand and in overall spin polarization. For BP86, BLYP, and TPSS, the  $\beta$ -spin population on the nitrosyl ligand is between 0.20 and 0.26. It increases to approximately 0.5 for OLYP and OPBE and to 0.55 for M06-L. For the hybrid functionals TPSSh and B3LYP, there is a  $\beta$ -spin population of 0.83 and 1.0, respectively, on the nitrosyl ligand. Note that the difference of ca. 0.3 between OLYP and OPBE on the one side and BP86, BLYP, and TPSS on the other is even larger than for the larger complexes, where the  $\beta$ -spin populations on the nitrosyl ligand differ only by approximately 0.2.

Thus, the magnitude of the differences between the different functionals is comparable to those found for complexes **1** and **2**.

Note that for **3**, three different states can be optimized in the SCF procedure. In general, the state corresponding to 16  $\alpha$  and 15  $\beta$  electrons in  $\text{A}'$  and 4  $\alpha$  and  $\beta$  electrons in  $\text{A}''$  represents the sought ground state that corresponds to the larger complexes, and all spin density distributions and in the following molecular orbitals are presented and discussed for this state. The energies obtained for all three possible states are given in Table 3 in the Supporting Information. Only with OPBE and B3LYP, the state corresponding to the larger complexes is not the ground state. Note that the point charges try to model a square planar ligand field in order to enforce similar occupation of orbitals in **3** as found in the larger  $\{\text{FeNO}\}^7$  complexes. For OPBE and B3LYP, however, the modeled ligand field is not strong enough, leading to a physically unreasonable ground state.

But what is the origin of the observed differences in spin density distributions? For the quartet state, all orbitals are similar for all exchange–correlation functionals considered, and thus, no dependence of the spin density distribution on the exchange–correlation functional is found. Furthermore, for all functionals, the resulting orbitals qualitatively agree with Hoffmann's simplified molecular orbital diagram and with the results obtained for the larger complexes **1** and **2**. In particular, the spin density is determined by the three singly occupied orbitals, which can be described as  $d_{xy}$ ,  $(d_{z^2}, \sigma)^*$ , and  $d_{x^2-y^2}$ . For the BP86 calculation, the relevant orbitals are shown in Figure 2b in the Supporting Information.

For the doublet configuration, the situation is different. An orbital analysis shows that the seven valence orbitals differ considerably for all selected exchange–correlation functionals. These seven orbitals determine the spin density distribution, which will be obvious if we refer to the orbital analysis of the larger  $\{\text{FeNO}\}^7$  complexes. As an explicit example, the orbitals for B3LYP, OLYP, and BP86 are shown in Figure 9. As expected,

they represent a combination of the Fe d with the NO  $\sigma$  and NO  $\pi^*$  orbitals. The orbital shapes obtained for OLYP and BP86 are similar to those of the corresponding orbitals of the larger  $\{\text{FeNO}\}^7$  complexes, and the divergent distributions of  $\alpha$  and  $\beta$  electron density are due to similar occupation patterns. As for the larger complexes,  $\alpha$  and  $\beta$  orbitals differ. While  $\alpha$  electrons are centered on the iron atom,  $\beta$  electrons are more delocalized on the NO fragment. This leads to the separation of  $\alpha$ - and  $\beta$ -electron density and results in weak spin polarization. The reduced  $\beta$ -electron density around the NO fragment obtained for BP86 is due to the enhanced delocalization of  $\alpha$  electrons into the  $\pi^*$  orbital as compared to OLYP for the ( $d_{yz}$ ,  $\pi^*$ ) and ( $d_{xz}$ ,  $\pi^*$ ) orbitals.

In the case of B3LYP, different orbital combinations are obtained, as we have already observed in **1**. The  $\alpha_1$  and  $\alpha_3$  and the  $\beta_1$  and  $\beta_3$  orbitals contain additional contributions from different Fe d orbitals as compared to OLYP or BP86. Furthermore,  $\alpha$  electrons preferentially occupy metal orbitals ( $\alpha_1$  to  $\alpha_4$ ), leading to an excess of  $\alpha$ -electron density on the iron atom, while  $\beta$  electrons are distributed over ligand  $\pi^*$  orbitals ( $\beta_1$  to  $\beta_3$ ), resulting in the corresponding excess of  $\beta$  electron density. This occupation pattern produces strong spin polarization in the B3LYP case. Compared to OLYP and BP86, different  $\alpha$  and  $\beta$  orbitals are obtained for B3LYP, resulting in a “broken-symmetry-like” solution, which we already observed for the larger  $\{\text{FeNO}\}^7$  complexes and which is also indicated by the expectation value of  $\langle S^2 \rangle$  of 1.48 compared to the ideal value of 0.75 (see also Table 2).

In conclusion, one observes that the DFT electronic structures of all complexes studied are similar and correspond to the qualitative molecular orbital diagram by Hoffmann: Similar orbital combinations and occupations are obtained. We observe a similar dependence of the spin density on the approximate exchange–correlation functional for complex **3** as for complexes **1** and **2**, and we can arrange the spin density distributions of **3** according to their spin density patterns in a similar way to what we found for complexes **1** and **2**. Furthermore, the differences in spin density distributions are based on similar reasons and can be traced back to the same differences in Kohn–Sham molecular orbitals. Hence, the  $[\text{Fe}(\text{NO})]^{2+}$  complex **3** can serve as a representative model system for the larger complexes **1** and **2**.

**4.2. CASSCF Calculations.** As discussed in the previous paragraph, the spin density distributions obtained for the doublet state of **3** are—as those of the larger complexes—dependent on the exchange–correlation functional, and it remains unclear which functional describes the spin density most accurately. To investigate this question, we calculated CASSCF reference spin densities. Since we consider a small model system in which the salen or porphyrin ligands have been removed and replaced by point charges, we can choose an active space that contains all orbitals that are possibly relevant for a correct description of the spin density.

In a minimal active space, all orbitals present in the qualitative molecular orbital diagram by Hoffmann et al. (see Figure 4) have to be included. This results in an active space which is composed of four Fe 3d orbitals ( $d_{xy}$ ,  $d_{xz}$ ,  $d_{yz}$ , and  $d_{z^2}$ ) and both NO  $\pi^*$  orbitals. In addition, the Fe  $d_{x^2-y^2}$  orbital has to be included. Altogether, this results in a minimal active space of seven electrons correlated in seven orbitals. As a further step, we also consider both NO  $\pi$  orbitals, which further extends the minimal active space to 11 electrons correlated in nine orbitals. The natural orbitals obtained in these minimal CAS(7,7) and

CAS(11,9) calculations are also shown in Figures 5 and 10 in the Supporting Information for the quartet and doublet states, respectively.

To guarantee that the spin density is converged with respect to the active space, we performed CASSCF calculations with different dimensions of the active space, which was systematically enlarged. In particular, it might be important to include an additional shell of Fe d orbitals (double-shell orbitals). The extension of the active orbital space by a second d-shell orbital for each metal 3d orbital represents a common procedure in CASSCF calculations.<sup>49,76</sup> However, it turns out that it is not trivial to identify these double-shell orbitals, because they mix considerably with antibonding ligand orbitals, and for this reason, additional antibonding ligand orbitals also have to be included in order to construct a stable active space.

For the quartet state, we proceed as follows. First, two virtual orbitals with contributions of Fe  $d_{xz}$  and  $d_{yz}$  were included in the CAS(11,9) active orbital space, resulting in the corresponding CAS(11,11) calculation. Yet, the  $d_{yz}$  double-shell orbital was rotated into an empty ligand orbital. To include this double-shell contribution, the active orbital space had to be extended by an additional virtual orbital, resulting in our CAS(11,12) calculation. The CAS(11,12) active space was further extended by an additional virtual orbital with a large contribution from the third Fe  $d_{z^2}$  orbital for the CAS(11,13) calculation. The fourth Fe  $d_{xy}$  double-shell orbital could be included in the active space in our CAS(11,15) calculation, which also contains an additional empty ligand orbital.

Similarly for the doublet state, first two virtual orbitals with contributions of Fe  $d_{xz}$  and  $d_{xy}$  were included in the CAS(11,9) described above, resulting in a CAS(11,11). Adding one additional virtual orbital with a contribution from Fe  $d_{yz}$  yields a CAS(11,12) active space. The fourth Fe  $d_{z^2}$  orbital could be included in our CAS(11,14) calculation, which contains an additional empty ligand orbital. Finally, we note that the contributions of the Fe double-shell orbitals to the natural orbitals are significantly larger for the doublet state than for the quartet state.

The CAS(11,15) and CAS(11,14) calculations for the quartet and doublet state, respectively, contain the four Fe  $d_{xz}$ ,  $d_{xy}$ ,  $d_{yz}$ , and  $d_{z^2}$  double-shell orbitals. Including the fifth (Fe  $d_{x^2-y^2}$ ) double-shell orbital was, however, not feasible since its destabilization by the point charge environment requires the including of a number of additional ligand orbitals. For both the quartet and the doublet state, we also explored CASSCF calculations in which we extended the CAS(11,11) active space by one ligand  $\sigma$  orbital and the corresponding antibonding  $\sigma^*$  orbital, resulting in a CAS(13,13) containing the Fe  $d_{xz}$  and  $d_{xy}$  double-shell orbitals. However, including the remaining Fe double-shell orbitals in these calculations turned out to be problematic and would require the inclusion of additional ligand orbitals. Therefore, calculations with an active space containing the four Fe double-shell orbitals, which are included in the CAS(11,15) or CAS(11,14) calculations, were not possible. For this reason, we will only consider the CAS(11, $x$ ) calculations in the following. The converged natural orbitals for all employed active spaces can be found in the Supporting Information (Figures 5–9 and 10–14 for the quartet and doublet states, respectively).

The CASSCF spin densities of the quartet and doublet states are shown in Figures 10a and 11a, respectively. For the quartet state, one finds only a weak dependence of the spin density on the size of the active space chosen, and the CASSCF spin density

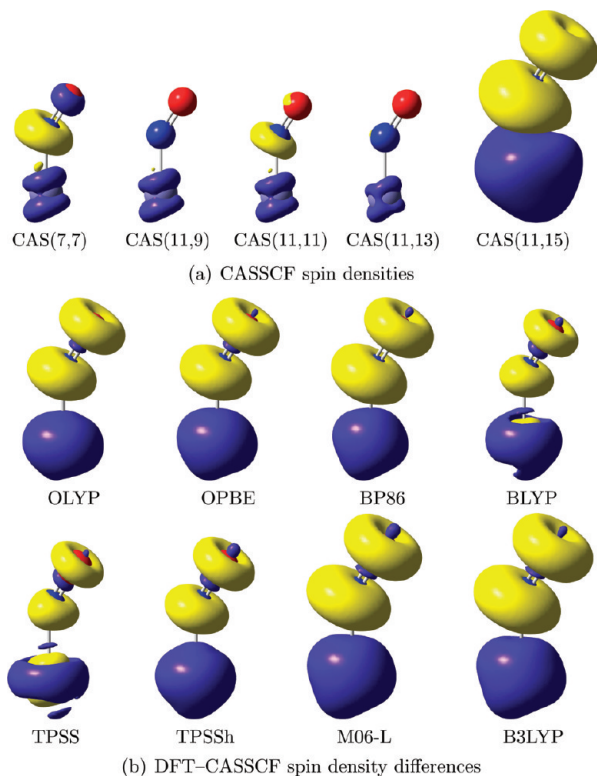


**Figure 10.** (a) CASSCF spin density difference plots for different dimensions of the active space with respect to the CAS(11,15) reference spin density for the quartet state of 3. The CAS(11,15) spin density is shown on the right-hand side. The blue surface corresponds to an excess of  $\alpha$ -electron density, while the yellow surface corresponds to an excess of  $\beta$ -electron density. (b) Difference plots of the spin density for the approximate exchange–correlation functionals and the CAS(11,15) reference spin density profile for the quartet state of  $[\text{Fe}(\text{NO})]^{2+}$ . An isosurface value of 0.003 is used throughout. Similar plots using larger isosurface values are included in the Supporting Information (Figures 17 and 18).

profiles are similar for all active spaces considered. Therefore, the figures only show the CAS(11,15) spin density, while for the smaller active spaces, only the difference with respect to CAS(11,15) is shown. For the CAS(7,7) and CAS(11,9) calculations (i.e., without double-shell effect), the spin density distributions are qualitatively in good agreement with our converged CAS(11,15) reference spin density. Hence, already these minimal active spaces are sufficient to obtain an accurate spin density distribution. We note that also for the active spaces containing 13 active electrons, only small differences in the spin density are found (see the difference spin density plots in Figure 15 of the Supporting Information).

For the doublet state, larger deviations of the spin density distribution with respect to the size of the active space can be observed. Figure 11a shows the spin-density differences with respect to the CAS(11,14) reference, for which the active space contains the four most important double-shell d orbitals. When enlarging the active space, the spin density gradually converges toward the CAS(11,14) reference. We should note that the CAS(7,7) and CAS(11,9) spin densities, i.e., for active spaces without double-shell orbitals, are qualitatively similar to the CAS(11,14) reference spin density. These minimal active spaces are sufficient to obtain a qualitative estimate of the spin density

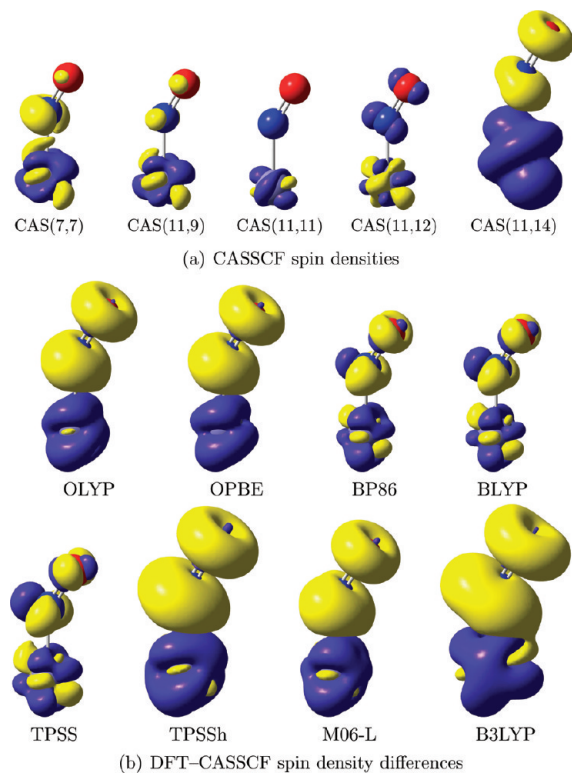


**Figure 11.** (a) CASSCF spin density difference plots for different active spaces with respect to the CAS(11,14) reference spin density for the doublet state of 3. The CAS(11,14) reference spin density is shown on the right-hand side. The blue surface (positive spin density) corresponds to an excess of  $\alpha$ -electron density, while the yellow surface (negative spin density) corresponds to an excess of  $\beta$ -electron density. (b) Difference plots of the spin density for the approximate exchange–correlation functionals and the CAS(11,14) reference spin density profile for the doublet state of  $[\text{Fe}(\text{NO})]^{2+}$ . An isosurface value of 0.003 is used throughout. Similar plots using larger isosurface values are included in the Supporting Information (Figures 19 and 20).

distribution, while for quantitatively correct spin densities, Fe double-shell orbitals have to be included. Again, also for the active spaces containing 13 active electrons, very similar spin densities are obtained (see the difference spin density plots in Figure 16 of the Supporting Information.)

To analyze the origin of the spin densities in the CASSCF calculations, we will examine the natural orbitals and CASSCF configurations of 3 in detail. An in-depth discussion on the electronic structure of the larger  $\{\text{FeNO}\}^7$  complexes can be found in ref 49. Concerning both the quartet and doublet states, the natural orbitals of different active spaces are in general similar; only some deviations in orbital shape and occupation numbers can be recognized when the active space is enlarged. The most important natural orbitals which correspond to those in the minimal active space of seven electrons in seven orbitals are shown in Figure 12. In general, the Fe  $d_{xy}$  orbital does not interact with the ligand orbitals for all active spaces considered. Moreover, we observe a strong covalent interaction between three Fe d orbitals ( $d_{yz}$ ,  $d_{xz}$ ,  $d_{z^2}$ ) and the NO  $\sigma$  and  $\pi^*$  orbitals resulting in two bonding [ $(d_{yz}, \pi^*)$  and  $(d_{xz}, \pi^*)$ ], two antibonding [ $(d_{yz}, \pi^*)^*$  and  $(d_{xz}, \pi^*)^*$ ], and one nonbonding orbital [ $(d_{z^2}, \sigma)^*$ ]. In general, the three highest bonding [ $(d_{yz}, \pi^*)$ ,  $(d_{xz}, \pi^*)$ , and  $d_{xy}$ ], the two lowest antibonding orbitals [ $(d_{yz}, \pi^*)^*$  and  $(d_{xz}, \pi^*)^*$ ], and

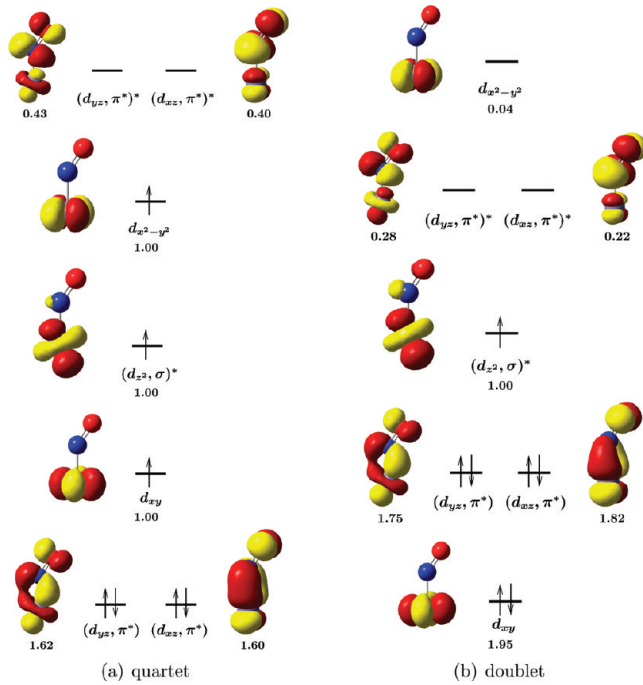


**Figure 12.** Natural orbitals and occupation numbers for the CAS(11,15) calculations of the quartet state and the CAS(11,14) calculation of the doublet configuration of 3. An isosurface value of 0.05 was chosen. The natural orbitals are printed according to their occupation number. The arrows indicate the occupation in the principal configuration.

additionally the  $(d_{z^2}, \sigma)^*$  orbital resemble qualitatively the orbital picture of Hoffmann et al., as given in Figure 4.

To identify how the spin density arises, one needs to investigate not only the (spin-independent) natural orbitals but also the corresponding wave functions. To this end, Table 3 lists the most important configurations for the quartet and the doublet states. For both the doublet and the quartet configuration, the CI coefficients are very similar for different active spaces, and therefore, only those obtained in the largest active spaces, CAS(11,15) for the quartet and CAS(11,14) for the doublet, are given in the table. For the quartet state, variations in CI coefficients are in general below 10%; only for the configuration with small CI weights can larger deviations be observed. Furthermore, there is a dominant contribution to the wave function (CI weight > 0.7) which corresponds to the quartet ground state; all other CI coefficients are smaller (<0.3). This principal configuration is also shown in Figure 12 and qualitatively corresponds to the orbitals obtained in the DFT calculations. The principal configuration, however, which contains three unpaired electrons on the iron atom, cannot explain the observed spin polarization (Figure 10a). The polarization can be accounted for by adding those configurations that contain excitations from the bonding  $(d_{yz}, \pi^*)$  and  $(d_{xz}, \pi^*)$  to the antibonding  $(d_{yz}, \pi^*)^*$  and  $(d_{xz}, \pi^*)^*$  orbitals, which shifts the  $\beta$ -electron density toward the ligand. All of these excitations correspond to medium-sized CI coefficients (>0.05) and are marked in bold face in Table 3. The distribution of  $\beta$  electrons in both NO  $\pi^*$  orbitals results in its characteristic cylindrical shape. Hence, these excited configurations lead to an excess of  $\alpha$ -electron density on the iron atom and an excess of  $\beta$ -electron density on the NO fragment. It should be noted that in all of the configurations listed in Table 3, the  $(d_{z^2}, \sigma)^*$ ,  $d_{xy}$  and  $d_{x^2-y^2}$  orbitals are each singly occupied by one  $\alpha$  electron.

**Table 3.** Total Wave Function for the Quartet State for the CAS(11,15) and for the Doublet State for the CAS(11,14) Calculation of 3<sup>a</sup>

	$S = (3/2)$	$S = (1/2)$	
22 aaa 00	0.7030268	2 22 a 00 0	0.8441848
20 aaa 20	-0.2427797	<b>2 ba a b 0</b>	-0.1388339
02 aaa 02	-0.2329925	<b>2 ab a bb 0</b>	-0.1239105
<b>2a aaa b0</b>	0.2081849	<b>2 aa b bb 0</b>	0.1021302
<b>a2 aaa 0b</b>	0.1955026	<b>2 2a b a 00</b>	-0.0859653
ab aaa ab	0.1355478	<b>2 bb a aa 0</b>	0.0844657
<b>0a aaa b2</b>	-0.0551488	<b>2 2a a b 00</b>	0.0747853

<sup>a</sup> On the left-hand side, the configurations are printed; on the right hand-side, the corresponding CI coefficients are given. Only those natural orbitals which are important for the spin density are considered; all other bonding orbitals are doubly occupied and all other antibonding orbitals empty. The orbital ordering corresponds to the one in Figure 12:  $(d_{yz}, \pi^*)$ ,  $(d_{xz}, \pi^*)$ ,  $d_{xy}$ ,  $d_{x^2-y^2}$ ,  $(d_{z^2}, \sigma)^*$ ,  $(d_{yz}, \pi^*)^*$ , and  $(d_{xz}, \pi^*)^*$  for the quartet state and  $d_{xy}$ ,  $(d_{yz}, \pi^*)$ ,  $(d_{xz}, \pi^*)$ ,  $(d_{z^2}, \sigma)^*$ ,  $(d_{yz}, \pi^*)^*$ ,  $(d_{xz}, \pi^*)^*$ , and  $d_{x^2-y^2}$  for the doublet state, respectively. Further, those configurations which are important for the spin density and correspond to CI coefficients larger than 0.05 are considered and marked in bold face. A more detailed table can be found in the Supporting Information. 2: doubly occupied orbital. a: orbital occupied by an  $\alpha$  electron. b: orbital occupied by a  $\beta$  electron. 0: empty orbital.

A similar observation can be made for the doublet configuration. As for the quartet state, there is one principal contribution to the wave function (CI weight > 0.8), which is included in Figure 12 and qualitatively corresponds to the orbitals obtained in the DFT calculations. In addition, we find configurations which correspond to excitations from the bonding  $(d_{yz}, \pi^*)$  and  $(d_{xz}, \pi^*)$  to the antibonding  $(d_{yz}, \pi^*)^*$  and  $(d_{xz}, \pi^*)^*$  orbitals. However, both  $\alpha$ - and  $\beta$ -electron excitations are present in configurations with large CI weights for the doublet configuration, while for the quartet state, configurations containing only excitations of  $\beta$  electrons correspond to large CI coefficients. These excitations are marked in bold face in Table 3. Admixture of these configurations leads to a weaker spin polarization for the doublet state as compared to the quartet state. Furthermore, for most configurations with large CI coefficients, the  $(d_{z^2}, \sigma)^*$  orbital remains singly occupied by an  $\alpha$  electron, which induces the characteristic shape of the  $\alpha$ -electron density around the Fe atom.

**4.3. Comparison of CASSCF and DFT Results.** The isosurface plot of the CASSCF reference spin densities in Figure 10a can be compared to those obtained from DFT calculations, shown in Figure 7. All considered exchange–correlation functionals favor spin polarization, and there is a good qualitative agreement between the DFT and CASSCF spin densities. However, a comparison of the isosurface plots might be misleading. Therefore, to consider a more quantitative benchmark of DFT spin density distributions as well, we additionally calculated difference plots of the DFT and CASSCF spin densities with respect to the CAS(11,15) spin density, which is shown in Figure 10b. Note that these difference plots employ the same isosurface value that was used for the spin densities themselves in Figures 7 and 10a. Plots using larger isosurface values are included in the Supporting Information. These spin density difference plots are very similar for all of the considered exchange–correlation functionals, but in all cases, there are non-negligible differences between DFT and CASSCF. At the

**Table 4.** Selected Mulliken Spin Populations for the Doublet State of 3

method	$S = 1/2$		
	Fe	N	O
OLYP	1.484	-0.259	-0.226
OPBE	1.520	-0.283	-0.237
BP86	1.259	-0.130	-0.129
BLYP	1.218	-0.105	-0.114
TPSS	1.208	-0.101	-0.107
TPSSh	1.831	-0.453	-0.378
M06-L	1.545	-0.294	-0.252
B3LYP	2.023	-0.559	-0.465
CAS(11,11)	1.168	-0.082	-0.086
CAS(11,12)	1.090	-0.036	-0.054
CAS(11,14)	1.144	-0.068	-0.076

nitrosyl ligand, all functionals predict a  $\beta$ -electron density that is too high, while at the Fe atom, there is a redistribution of the  $\alpha$ -electron density. However, the shape of these spin density differences is comparable to that of the spin density itself, which indicates that the differences are mainly quantitative. While the shape of the spin density is qualitatively correct with all functionals, they all overestimate the spin polarization. This overestimation is the smallest for the BP86, BLYP, and TPSS functionals.

Similarly for the doublet state, a qualitative estimate of the accuracy of approximate exchange–correlation functionals can be obtained by comparing the DFT and CASSCF spin density isosurface plots in Figures 7 and 11a, respectively. In the CASSCF calculations, the  $\alpha$ -electron density is located at the iron atom, while on the nitrosyl ligand, there is only  $\beta$ -electron density, with an almost cylindrical shape. By contrast, the spin densities obtained with BP86, BLYP, and TPSS contain  $\alpha$ -electron density close to the nitrogen atom. Thus, the spin densities obtained with these functionals disagree with the accurate CASSCF spin density. For all other functionals, the isosurface plots qualitatively appear to agree with the CASSCF reference spin density.

However, in contrast to this apparently good agreement of the DFT and CASSCF isosurface plots for all functionals except BP86, BLYP, and TPSS, we can observe considerable differences in the corresponding DFT–CASSCF spin-density difference plots in Figure 11b. With OLYP, OPBE, and M06-L, there is a too large  $\beta$ -electron density on the nitrosyl ligand, and a too large  $\alpha$ -electron density at the Fe atom; i.e., the spin polarization is overestimated. The magnitude of these differences is comparable to the one found for the quartet state. The hybrid functionals TPSSh and B3LYP yield an even larger excess of  $\beta$  electrons at the nitrosyl fragment and an overall larger spin polarization compared to the CASSCF reference. As discussed above, this is due to the “broken-symmetry-like” solutions obtained in this case. Finally, for BP86, BLYP, and TPSS, where already the isosurface plots of the spin density itself did qualitatively not agree with the CASSCF reference, the difference plots reveal a too large  $\beta$ -electron density on the nitrosyl ligand, with a redistribution of spin density close to the nitrogen. However, even though there is a qualitative disagreement close to the nitrogen atom, the smallest differences from the CASSCF reference spin density are found for the BP86, BLYP, and TPSS exchange–correlation functionals.

A similar picture can be obtained from comparing Mulliken spin populations of the DFT and CASSCF calculations given in Table 4. These also show that the functionals can be arranged in three groups: For BP86, BLYP, and TPSS, the Mulliken spin populations agree best. A slightly worse agreement is found for OLYP, OPBE, and M06-L. And, a much larger deviation from the CASSCF reference is found for B3LYP and TPSSh. Note, however, that a comparison of Mulliken spin populations obtained in different basis sets (Slater-type TZP basis set for DFT and Gaussian-type cc-pVTZ for CASSCF) is problematic. Despite the good agreement of the Mulliken spin populations for BP86, BLYP, and TPSS, the spin density difference plots show that for all functionals there are significant deviations from the CASSCF spin density.

These deviations in spin densities can also be related to differences in CASSCF and DFT orbitals. However, it is important to realize that such a comparison can be misleading: DFT and CASSCF both try to represent the same (spin) density in a different fashion (i.e., with integer and noninteger occupation numbers, respectively). Therefore, even with the exact exchange–correlation functional, the Kohn–Sham orbitals and the CASSCF natural orbitals would differ. The CASSCF natural orbitals are in general more delocalized than the corresponding DFT orbitals, in particular around the NO ligand (NO  $\pi^*$  orbitals), which decreases the  $\alpha$ -electron density around the Fe atom. This can be observed as the blue surface in the spin density difference plots. The larger (or smaller) distribution of  $\beta$  electrons around the NO ligand with respect to the CASSCF reference can refer to the stronger (or weaker) delocalization of  $\beta$  electrons in the NO  $\pi^*$  orbitals. Note that the CASSCF excitation structure decreases the  $\beta$ -electron density around the NO ligand and simultaneously the  $\alpha$ -electron density around the Fe atom.

In summary, the comparison of DFT and CASSCF spin densities shows that none of the exchange–correlation functionals considered here is able to predict the spin density distributions accurately. This view is supported by a comparison of the spin density isosurface plots, the spin density difference plots, and a comparison of the Mulliken spin populations. The size of the differences in the spin density is comparable for the quartet state and for the doublet state. For both the quartet and the doublet states, the smallest differences are found with the BP86, BLYP, and TPSS exchange–correlation functionals, even though for the doublet state these three functionals result in a qualitatively wrong spin density close to the nitrogen atom.

## 5. CONCLUSIONS

Since the spin density represents an essential quantity for the calculation of EPR parameters, it is important for quantum chemistry to be able to predict spin density distributions reliably. Recently, Conradie and Ghosh<sup>31</sup> discussed the difficulty in calculating accurate spin density distributions for  $\{\text{FeNO}\}^7$  complexes employing DFT<sup>31</sup> where different exchange–correlation functionals yield qualitatively very different spin density distributions. In this work, we extend their studies by considering a large representative set of exchange–correlation functionals and by performing a detailed orbital analysis of the sources of the resulting differences in spin densities.

For the  $\{\text{FeNO}\}^7$  complexes, the DFT description of the low-spin doublet state remains most challenging. The spin density distributions are sensitive to the chosen approximate exchange–correlation functional. Our orbital analysis shows that the

different spin densities can be traced back to different occupation patterns with respect to only a few orbitals. The seven highest molecular orbitals turn out to be crucial for the distribution of  $\alpha$  and  $\beta$  electrons. Especially, the differences in the two ( $d, \pi^*$ ) orbitals and the ( $d_{z^2}, \sigma$ ) $^*$  orbital explain the spin density distribution obtained for nonhybrid exchange–correlation functionals. The hybrid functional B3LYP, however, results in a “broken-symmetry-like” solution. This shows that one has to be very careful when considering spin densities of low-spin states obtained from DFT calculations. If no “broken-symmetry-like” solution is obtained (as in the case of the nonhybrid functionals), the spin density can be interpreted as an approximation to the real spin density. If, on the other hand, a “broken-symmetry-like” solution is obtained, the DFT spin density does not correspond to the physical spin density. Instead, it could be interpreted as an approximation to the on-top pair density.<sup>38</sup> However, this precludes the calculation of properties depending on the spin density such as EPR parameters and is thus not desirable.

To decide which approximate exchange–correlation functionals yield accurate spin density distributions, multireference methods are required. Comparison to CASSCF results can serve as an accurate benchmark of exchange–correlation functionals. However, for the large complexes, it is not a priori clear whether the active spaces that are computationally feasible include all of the relevant orbitals. Therefore, we introduced a small model molecule,  $[\text{Fe}(\text{NO})]^{2+}$ , which features the same electronic structure and exhibits a similar dependence of the spin density on the approximate exchange–correlation functional as the larger complexes. Due to its small size, we can efficiently apply the CASSCF approach. Furthermore, we can employ an active space that includes all relevant orbitals that have metal–ligand character as well as four of the five Fe double-shell d orbitals. This results in an active space of 11 electrons correlated in 15 or 14 active orbitals, which appears to be sufficient to obtain reliable reference spin densities.

Note that while such rather small active spaces are sufficient for the small  $[\text{Fe}(\text{NO})]^{2+}$  model system to obtain converged spin density distributions, this might not be the case for the salen and porphyrin complexes anymore. CASSCF calculations for different  $\{\text{FeNO}\}^7$  complexes and medium-sized active spaces have already been presented in the literature,<sup>49</sup> giving first insights into the quality of DFT spin densities. However, studying the convergence of the spin density with respect to the dimension of the active space for these larger complexes remains challenging since additional ligand and iron orbitals should be included in the active space.<sup>49</sup> This renders such calculations infeasible with standard correlation methods. An efficient treatment of larger active spaces is possible with conceptually different electronic correlation methods such as the DMRG algorithm.<sup>77–79</sup> The DMRG study of the discussed  $\{\text{FeNO}\}^7$  complexes is part of our future work.

A comparison of DFT and CASSCF spin density isosurface plots for the quartet state indicates that DFT provides qualitatively consistent spin densities for all exchange–correlation functionals studied. However, an inspection of DFT–CASSCF spin density difference plots shows non-negligible differences. These are similar for all exchange–correlation functionals, where the smallest differences are observed for the BP86, BLYP, and TPSS functionals. The deviations are mainly in the quantitative description of the amount of spin polarization, while qualitatively, the spin density is predicted correctly.

For the doublet state, the spin densities obtained with different exchange–correlation functionals are very different. The best agreement is again found for BP86, BLYP, and TPSS. However, these three functionals predict a qualitatively different spin density distribution at the ligand nitrogen atom. The spin densities obtained with the remaining nonhybrid functionals show larger deviations and predict a too large spin polarization, whereas the hybrid functionals B3LYP and TPSH result in a “broken-symmetry-like” solution with a qualitatively wrong spin density. These results agree with those of earlier work by Pierloot et al.,<sup>49</sup> who found that for the doublet states of the larger  $\{\text{FeNO}\}^7$  complexes, nonhybrid functionals yield spin densities which are (on the basis of a comparison of spin density isosurface plots and Mulliken spin populations) in closest agreement with the CASSCF reference.

In summary, we find that none of the tested exchange–correlation functionals is able to provide a satisfactory description of the spin densities in the considered iron nitrosyl complexes. Hence, improved exchange–correlation functionals that reliably predict the spin densities in transition metal complexes will have to be developed. Our results indicate that the currently available functionals do not take the spin density (which is, in addition to the total density, a basic variable in spin-DFT) properly into account. Therefore, we believe that considering the spin density more closely provides a promising route to improved exchange–correlation functionals for transition metal chemistry.

## ■ ASSOCIATED CONTENT

**S Supporting Information.** Additional details on orbitals and active spaces are available and have been included. This information is available free of charge via the Internet at <http://pubs.acs.org/>.

## ■ AUTHOR INFORMATION

### Corresponding Authors

\*E-mail: christoph.jacob@kit.edu, markus.reiher@phys.chem.ethz.ch.

## ■ ACKNOWLEDGMENT

Financial support by the Swiss National Science Foundation (SNF) is gratefully acknowledged (project 200020-132542/1). C.R.J. acknowledges funding from the DFG-Center of Functional Nanostructures in Karlsruhe. K.B. thanks the Fonds der Chemischen Industrie for a Chemiefonds scholarship.

## ■ REFERENCES

- (1) Carreira, E. M.; Kvaerno, L. *Classics in Stereoselective Synthesis*, 1st ed.; Wiley-VCH: Weinheim, Germany, 2009.
- (2) Valentine, J. S.; Poulos, T. L.; Jameson, G. B.; Ibers, J. A.; Que, L., Jr.; Yoshikawa, S.; Lindley, P. F. Oxygen Metabolism. In *Biological Inorganic Chemistry: Structure and Reactivity*, 1st ed.; Gray, H. B., Stiebel, E. I., Valentine, J. S., Bertini, I., Eds.; University Science Book: Sausalito, CA, 2007; pp 319–442.
- (3) Frenking, G.; Fröhlich, N. *Chem. Rev.* **2000**, *100*, 717.
- (4) Ziegler, T.; Autschbach, J. *Chem. Rev.* **2005**, *105*, 2695.
- (5) Neese, F. *Coord. Chem. Rev.* **2009**, *293*, 526.
- (6) Rozanska, X.; Sauer, J. *J. Phys. Chem. A* **2009**, *113*, 11586.
- (7) Sillar, K.; Hofmann, A.; Sauer, J. *J. Am. Chem. Soc.* **2009**, *131*, 4143.

- (8) Trinh, C.; Timoshkin, A. Y.; Frenking, G. *J. Phys. Chem. A* **2009**, *113*, 3420.
- (9) Duarte, F. J. S.; Cabrita, E. J.; Frenking, G.; Santos, A. G. *Chem.—Eur. J.* **2009**, *15*, 1734.
- (10) Fan, J.; Autschbach, J.; Ziegler, T. *Inorg. Chem.* **2010**, *49*, 1355.
- (11) Podewitz, M.; Reiher, M. *Adv. Inorg. Chem.* **2010**, *62*, 177.
- (12) Podewitz, M.; Stiebrtz, M. T.; Reiher, M. *Faraday Discuss.* **2011**, *148*, 119.
- (13) Reiher, M. *Chimia* **2009**, *63*, 140.
- (14) Reiher, M. *Faraday Discuss.* **2007**, *135*, 97.
- (15) Reiher, M.; Sellmann, D.; Hess, B. A. *Theor. Chem. Acc.* **2001**, *106*, 379.
- (16) Reiher, M. *Inorg. Chem.* **2002**, *41*, 6928.
- (17) Herrmann, C.; Yu, L.; Reiher, M. *J. Comput. Chem.* **2006**, *27*, 1223.
- (18) Zein, S.; Borshch, S. A.; Fleurat-Lessard, P.; Casida, M. E.; Chermette, H. *J. Chem. Phys.* **2007**, *126*, 014105.
- (19) Fouqueau, A.; Casida, M. E.; Daku, L. M. L.; Hauser, A.; Neese, F. *J. Chem. Phys.* **2005**, *122*, 044110.
- (20) Fouqueau, A.; Mer, S.; Casida, M. E.; Daku, L. M. L.; Hauser, A.; Mineva, T.; Neese, F. *J. Chem. Phys.* **2004**, *120*, 9473.
- (21) Daku, L. M. L.; Vargas, A.; Hauser, A.; Fouqueau, A.; Casida, M. E. *ChemPhysChem* **2005**, *6*, 1393.
- (22) Ganzenmüller, G.; Berkaine, N.; Fouqueau, A.; Casida, M. E.; Reiher, M. *J. Chem. Phys.* **2005**, *122*, 234321.
- (23) Paulsen, H.; Trautwein, A. X. *Top. Curr. Chem.* **2004**, *235*, 197.
- (24) Swart, M. *J. Chem. Theory Comput.* **2008**, *4*, 2057.
- (25) Ye, S.; Neese, F. *Inorg. Chem.* **2010**, *49*, 772.
- (26) Reiher, M.; Salomon, O.; Hess, B. A. *Theor. Chem. Acc.* **2001**, *107*, 48.
- (27) Cramer, C. J.; Truhlar, D. G. *Phys. Chem. Chem. Phys.* **2009**, *11*, 10757.
- (28) Salomon, O.; Reiher, M.; Hess, B. A. *J. Comput. Chem.* **2002**, *117*, 4729.
- (29) Bachler, V.; Olbrich, G.; Neese, F.; Wieghardt, K. *Inorg. Chem.* **2002**, *41*, 4179.
- (30) Ghosh, A. *J. Biol. Inorg. Chem.* **2006**, *11*, 712.
- (31) Conradie, J.; Ghosh, A. *J. Phys. Chem. B* **2007**, *111*, 12621.
- (32) Radon, M.; Pierloot, K. *J. Phys. Chem. A* **2008**, *112*, 11824.
- (33) Jensen, K. P.; Cirera, J. *J. Phys. Chem. A* **2009**, *113*, 10033.
- (34) Olah, J.; Harvey, J. N. *J. Phys. Chem. A* **2009**, *113*, 7338.
- (35) Hohenberg, P.; Kohn, W. *Phys. Rev.* **1964**, *136*, B864.
- (36) Parr, R. G.; Yang, W. Spin-density-functional theory. In *Density-Functional Theory of Atoms and Molecules*, 1st ed.; Breslow, R., Goodenough, J. B., Halpern, J., Rowlinson, J. S., Eds.; Oxford University Press, Inc.: New York, 1989; pp 169–174.
- (37) von Barth, U.; Hedin, L. *J. Phys. C* **1972**, *5*, 1629.
- (38) Perdew, J. P.; Ruzsinszky, A.; Constantin, L. A.; Sun, J.; Csonka, G. I. *J. Chem. Theory Comput.* **2009**, *5*, 902.
- (39) Pople, J. A.; Gill, P. M. W.; Handy, N. C. *Int. J. Quantum Chem.* **1995**, *56*, 303.
- (40) Munzarová, M. L.; Engels, B.; Rassolov, V. A.; Chipman, D. M.; Patchkovskii, S.; Schreckenbach, G.; Lushington, G. H.; Neese, F. EPR Parameters, Methodological Aspects. In *Calculation of NMR and EPR Parameters. Theory and Applications*, 1st ed.; Kaupp, M., Bühl, M., Malkin, V. G., Eds.; Wiley-VCH: Weinheim, Germany, 2004; pp 461–564.
- (41) Munzarová, M. L.; Kubáček, P.; Kaupp, M. *J. Am. Chem. Soc.* **2000**, *122*, 11900.
- (42) van Lenthe, E.; van der Avoird, A.; Wormer, P. E. S. *J. Comput. Chem.* **1998**, *108*, 4783.
- (43) Neese, F. *J. Chem. Phys.* **2003**, *118*, 3939.
- (44) Szilagyi, R. K.; Metz, M.; Solomon, E. I. *J. Phys. Chem. A* **2002**, *106*, 2994.
- (45) Kossmann, S.; Kirchner, B.; Neese, F. *Mol. Phys.* **2007**, *105*, 2040.
- (46) Perdew, J. P.; Savin, A.; Burke, K. *Phys. Rev. A* **1995**, *51*, 4531.
- (47) Radon, M.; Broclawik, E. *J. Chem. Theory Comput.* **2007**, *3*, 728.
- (48) Roos, B. O.; Veryazov, V.; Conradie, J.; Taylor, P. R.; Ghosh, A. *J. Phys. Chem. B* **2008**, *112*, 14099.
- (49) Radon, M.; Broclawik, E.; Pierloot, K. *J. Phys. Chem. B* **2010**, *114*, 1518.
- (50) Velde, G. T.; Bickelhaupt, F. M.; Baerends, E. J.; Guerra, C. F.; van Gisbergen, S. J. A.; Snijders, J. G.; Ziegler, T. *J. Comput. Chem.* **2001**, *22*, 931.
- (51) Becke, A. D. *J. Chem. Phys.* **1993**, *98*, 5648.
- (52) Perdew, J. P.; Tao, J.; Staroverov, V. N.; Scuseria, G. E. *J. Chem. Phys.* **2003**, *119*, 12129.
- (53) Handy, N. C.; Cohen, A. *J. Mol. Phys.* **2000**, *99*, 403.
- (54) Perdew, J. P.; Burke, K.; Ernzerhof, M. *Phys. Rev. Lett.* **1996**, *77*, 3865.
- (55) Perdew, J. P.; Burke, K.; Ernzerhof, M. *Phys. Rev. Lett.* **1997**, *78*, 1396.
- (56) Becke, A. D. *Phys. Rev. A* **1988**, *38*, 3098.
- (57) Perdew, J. P. *Phys. Rev. B* **1986**, *33*, 8822.
- (58) Lee, C.; Yang, W.; Parr, R. G. *Phys. Rev. B* **1988**, *37*, 785.
- (59) Perdew, J. P.; Tao, J.; Staroverov, V. N.; Scuseria, G. E. *Phys. Rev. Lett.* **2003**, *91*, 146401.
- (60) Zhao, Y.; Truhlar, D. G. *J. Chem. Phys.* **2006**, *125*, 194101.
- (61) Güell, M.; Luis, J. M.; Solà, M.; Swart, M. *J. Phys. Chem. A* **2008**, *112*, 6384.
- (62) ADF-GUI, version 2009.1; Scientific Computing and Modeling: Amsterdam, The Netherlands, 2009. See <http://www.scm.com> (accessed on July 31, 2011).
- (63) Werner, H.-J.; Knowles, P. J.; Lindh, R.; Manby, F. R.; Schütz, M.; Celani, P.; Korona, T.; Mitrushenkov, A.; Rauhut, G.; Adler, T. B.; Amos, R. D.; Bernhardsson, A.; Berning, A.; Cooper, D. L.; Deegan, M. J. O.; Dobbyn, A. J.; Eckert, F.; Goll, E.; Hampel, C.; Hetzer, G.; Hrenar, T.; Knizia, G.; Köpli, C.; Liu, Y.; Lloyd, A. W.; Mata, R. A.; May, A. J.; McNicholas, S. J.; Meyer, W.; Mura, M. E.; Nicklass, A.; Palmieri, P.; Pfüger, K.; Pitzer, R.; Reiher, M.; Schumann, U.; Stoll, H.; Stone, A. J.; Tarroni, R.; Thorsteinsson, T.; Wang, M.; Wolf, A. MOLPRO, version 2009.1; Cardiff University: Cardiff, United Kingdom; University of Stuttgart: Stuttgart, Germany, 2008.
- (64) T. H. Dunning, *J. Chem. Phys.* **1989**, *90*, 1007.
- (65) Balabanov, N. B.; Peterson, K. A. *J. Chem. Phys.* **2005**, *123*, 064107.
- (66) Werner, H.-J.; Meyer, W. *J. Chem. Phys.* **1981**, *74*, 5794.
- (67) Werner, H.-J.; Knowles, P. *J. Chem. Phys.* **1985**, *82*, 5053.
- (68) Knowles, P. J.; Werner, H.-J. *Chem. Phys. Lett.* **1985**, *115*, 259.
- (69) Varetto, U. Molekel, version 4.3; Swiss National Supercomputing Centre: Manno, Switzerland, 2000. See <http://molekel.csccs.ch/wiki/pmwiki.php>. (accessed on July 31, 2011).
- (70) Westcott, B. L.; Enemark, J. L. Transition Metal Nitrosyls. In *Inorganic Electronic Structure and Spectroscopy*; Solomon, E. I., Lever, A. B. P., Eds.; Wiley: New York, 1999; Vol. 2, pp 403–450.
- (71) Praneeth, V. K. K.; Neese, F.; Lehnert, N. *Inorg. Chem.* **2005**, *44*, 2570.
- (72) Praneeth, V. K. K.; Nalther, C.; Peters, G.; Lehnert, N. *Inorg. Chem.* **2006**, *45*, 2795.
- (73) Wells, F. V.; McCann, S. W.; Wickman, H. H.; Kessel, S. L.; Hendrickson, D. N.; Feltham, R. D. *Inorg. Chem.* **1982**, *21*, 2306.
- (74) Hoffmann, R.; Chen, M.-L.; Thorn, D. L. *Inorg. Chem.* **1977**, *16*, 503.
- (75) Hoffmann, R.; Chen, M.-L.; Elian, M.; Rossi, A. R.; Mingos, M. P. *Inorg. Chem.* **1974**, *13*, 2666.
- (76) Chen, H.; Song, J.; Lai, W.; Wu, W.; Shaik, S. *J. Chem. Theory Comput.* **2010**, *6*, 940.
- (77) Schollwöck, U. *Rev. Mod. Phys.* **2005**, *77*, 259.
- (78) Chan, G. K.-L.; Dorando, J. J.; Ghosh, D.; Hachmann, J.; Neuscamman, E.; Wang, H.; Yanai, T. An Introduction to the Density Matrix Renormalization Group Ansatz in Quantum Chemistry. In *Frontiers in Quantum Systems in Chemistry and Physics*, 1st ed.; Wilson, S., Grout, P. J., Maruani, J., Delgado-Barrio, G., Piecuch, P., Eds.; Springer: Dordrecht, The Netherlands, 2008; Vol. 18, pp 49–65; e-print: arXiv:0711.1398v1.
- (79) Marti, K. H.; Reiher, M. *Z. Phys. Chem.* **2010**, *224*, 583.